

Mixed Weyl semimetals and dissipationless magnetization control in insulators

Jan-Philipp Hanke,* Frank Freimuth, Chengwang Niu, Stefan Blügel, and Yuriy Mokrousov
*Peter Grünberg Institut and Institute for Advanced Simulation,
 Forschungszentrum Jülich and JARA, 52425 Jülich, Germany*
 (Dated: January 27, 2017)

We predict that the strength of spin-orbit torques and the Dzyaloshinskii-Moriya interaction in topologically non-trivial magnetic insulators can exceed significantly that of conventional metallic magnets. In analogy to the quantum anomalous Hall effect, we explain this extraordinary response in absence of longitudinal currents as a hallmark of magnetic monopoles in the electronic structure of systems that are interpreted most naturally within the framework of *mixed Weyl semimetals*. Remarkably, the magnetization switching by anti-damping torques in mixed Weyl semimetals can induce topological phase transitions due to the non-trivial interplay between magnetization direction and momentum-space topology. The concepts presented here may be exploited to understand and utilize magnetoelectric coupling phenomena in insulating ferromagnets and antiferromagnets.

Progress in control and manipulation of the magnetization in magnetic materials is pivotal for the innovative design of future non-volatile, high-speed, low power, and scalable spintronic devices. The effect of spin-orbit torque (SOT) provides an efficient means of magnetization control by electrical currents in systems that combine broken spatial inversion symmetry and spin-orbit interaction [1–5]. These current-induced torques are believed to play a key role in the practical implementation of various spintronics concepts, since they were demonstrated to mediate the switching of single ferromagnetic layers [6, 7] and antiferromagnets [8] via the exchange of spin angular momentum between the crystal lattice and the (staggered) collinear magnetization. Among the two different contributions to SOTs, the so-called anti-damping torques are of utter importance owing to the robustness of their properties with respect to details of disorder [5].

In a clean sample, the anti-damping SOT \mathbf{T} acting on the magnetization in linear response to the electric field \mathbf{E} is mediated by the so-called torkance tensor τ , i.e., $\mathbf{T} = \tau \mathbf{E}$ [9]. The Berry phase nature of the anti-damping SOT manifests in the fact that the tensor elements τ_{ij} are proportional to the *mixed* Berry curvature $\Omega_{ij}^{\hat{\mathbf{m}}\mathbf{k}} = \hat{\mathbf{e}}_i \cdot 2\text{Im} \sum_n^{\text{occ}} \langle \partial_{\hat{\mathbf{m}}} u_{\mathbf{k}n} | \partial_{k_j} u_{\mathbf{k}n} \rangle$ of all occupied states [9, 10], which incorporates derivatives of lattice-periodic wave functions $u_{\mathbf{k}n}$ with respect to both crystal momentum \mathbf{k} and magnetization direction $\hat{\mathbf{m}}$. Here, $\hat{\mathbf{e}}_i$ denotes the i th Cartesian unit vector. Intimately related to the anti-damping SOT is the Dzyaloshinskii-Moriya interaction (DMI) [11, 12], crucial for the emergence of chiral domain walls and chiral skyrmions [13–16], which can be quantified by the so-called spiralization tensor D reflecting the change of the free energy F due to chiral perturbations $\partial_j \hat{\mathbf{m}}$ according to $F = \sum_{ij} D_{ij} \hat{\mathbf{e}}_i \cdot (\hat{\mathbf{m}} \times \partial_j \hat{\mathbf{m}})$ [9].

Optimizing the efficiency of magnetization switching in spintronic devices by current-induced SOTs relies crucially on the knowledge of the microscopic origin of most prominent contributions to the electric-field response. To promote the understanding, it is rewarding to draw an analogy between the anti-damping SOT as given by $\Omega_{ij}^{\hat{\mathbf{m}}\mathbf{k}}$ and the intrinsic anomalous Hall effect as determined by the Berry curvature $\Omega_{ij}^{\mathbf{k}\mathbf{k}} = 2\text{Im} \sum_n^{\text{occ}} \langle \partial_{k_i} u_{\mathbf{k}n} | \partial_{k_j} u_{\mathbf{k}n} \rangle$ [17]. Both $\Omega_{ij}^{\mathbf{k}\mathbf{k}}$ and $\Omega_{ij}^{\hat{\mathbf{m}}\mathbf{k}}$ are components of a general curvature tensor Ω in the

composite $(\mathbf{k}, \hat{\mathbf{m}})$ phase space combining crystal momentum and magnetization direction [18, 19]. Band crossings, also referred to as magnetic monopoles in \mathbf{k} -space, are known to act as important sources or sinks of $\Omega^{\mathbf{k}\mathbf{k}}$ [20]. When transferring this concept to current-induced torques, crossing points in the composite phase space can be anticipated to give rise to a large mixed Berry curvature $\Omega^{\hat{\mathbf{m}}\mathbf{k}}$, which in turn yields the dominant microscopic contribution to torkance and spiralization. Thus, materials providing such monopoles can be expected to exhibit notably strong SOTs and DMI.

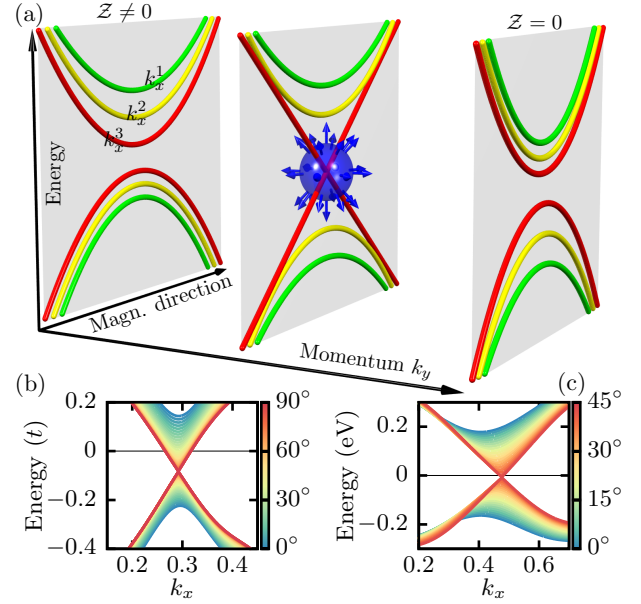


Figure 1. (Color online) (a) Schematic evolution of two energy bands in the complex phase space of crystal momentum and magnetization direction, where the colors of the bands indicate different k_x . If k_y is tuned, the electronic structure displays a monopole, which is correlated with a change in the mixed Chern number \mathcal{Z} . Such crossing points are observed in (b) the model of magnetically doped graphene with hopping t , and (c) the functionalized bismuth film, where colors indicate the magnetization direction $\hat{\mathbf{m}} = (\sin \theta, 0, \cos \theta)$. The shown monopoles arise at $\theta = 90^\circ$ and $\mathbf{k} = (0.29 \frac{2\pi}{a_x}, 0.41 \frac{2\pi}{a_y})$ for (b), and $\theta = 43^\circ$ and $\mathbf{k} = (0.48, 0.19)$ in internal units for (c).

In the field of topological condensed matter [21, 22], the recent advances in the realization of quantum anomalous Hall, or, Chern insulators have been striking [23, 24]. These magnetic materials are characterized by a quantized value of the anomalous Hall conductivity and an integer non-zero value of the Chern number in \mathbf{k} -space, $\mathcal{C} = 1/(2\pi) \int \Omega_{xy}^{kk} dk_x dk_y$. On the other hand, topological semimetals have recently attracted great attention due to their exceptional properties stemming from monopoles in momentum space. Among these latter systems, magnetic Weyl semimetals host gapless low-energy excitations with linear dispersion in the vicinity of non-degenerate band crossings at generic \mathbf{k} -points [25–28], which are sources of Ω^{kk} . Their conventional description in terms of the Weyl Hamiltonian can be formally extended to the case of what we call the *mixed Weyl semimetal* as described by $H_W = v_x k_x \sigma_x + v_y k_y \sigma_y + v_\theta \theta \sigma_z$, where θ is the angle that the magnetization $\hat{\mathbf{m}} = (\sin \theta, 0, \cos \theta)$ makes with the z -axis. As illustrated in Fig. 1a, mixed Weyl semimetals feature monopoles in the composite phase space of \mathbf{k} and θ , which are sources of the general curvature Ω . In analogy to conventional Weyl semimetals [25], we can characterize the topology and detect magnetic monopoles by monitoring the flux of the mixed Berry curvature through planes of constant k_y as given by the integer *mixed* Chern number $\mathcal{Z} = 1/(2\pi) \int \Omega_{yx}^{\hat{\mathbf{m}}\mathbf{k}} d\theta dk_x$, Fig. 1a. A significant electric-field response near monopoles in mixed Weyl semimetals would be invaluable in paving the road towards dissipationless magnetization control by SOTs [29].

In this Letter, using model arguments and first-principles calculations [30–35], we investigate the origin and size of anti-damping SOTs and DMI in representative topologically non-trivial magnetic insulators: (i) magnetically doped graphene, and (ii) a functionalized bismuth film. We demonstrate that these systems can be naturally interpreted as realizations of mixed Weyl semimetals in the composite phase space of \mathbf{k} and $\hat{\mathbf{m}}$. To characterize the anti-damping SOTs, we evaluate within linear response the torkance [9]

$$\tau_{ij} = \frac{2e}{N_{\mathbf{k}}} \hat{\mathbf{e}}_i \cdot \sum_{\mathbf{k}n}^{\text{occ}} [\hat{\mathbf{m}} \times \text{Im} \langle \partial_{\hat{\mathbf{m}}} u_{\mathbf{k}n} | \partial_{k_j} u_{\mathbf{k}n} \rangle], \quad (1)$$

where $N_{\mathbf{k}}$ is the number of \mathbf{k} -points, and $e > 0$ denotes the elementary positive charge. Similarly, the spiralization [9] is obtained as

$$D_{ij} = \frac{\hat{\mathbf{e}}_i}{N_{\mathbf{k}} V} \cdot \sum_{\mathbf{k}n}^{\text{occ}} [\hat{\mathbf{m}} \times \text{Im} \langle \partial_{\hat{\mathbf{m}}} u_{\mathbf{k}n} | h_{\mathbf{k}n} | \partial_{k_j} u_{\mathbf{k}n} \rangle], \quad (2)$$

where $h_{\mathbf{k}n} = H_{\mathbf{k}} + \mathcal{E}_{\mathbf{k}n} - 2\mathcal{E}_F$, $H_{\mathbf{k}}$ is the lattice-periodic Hamiltonian with eigenenergies $\mathcal{E}_{\mathbf{k}n}$, \mathcal{E}_F is the Fermi level, and V is the unit cell volume. Remarkably, we find that the magnitude of SOTs and DMI in the considered family of insulators can reach gigantic values exceeding by far that of conventional metallic ferromagnets. We show that emergent magnetic monopoles as sources of a large mixed Berry curvature in the composite phase space are pivotal in giving rise

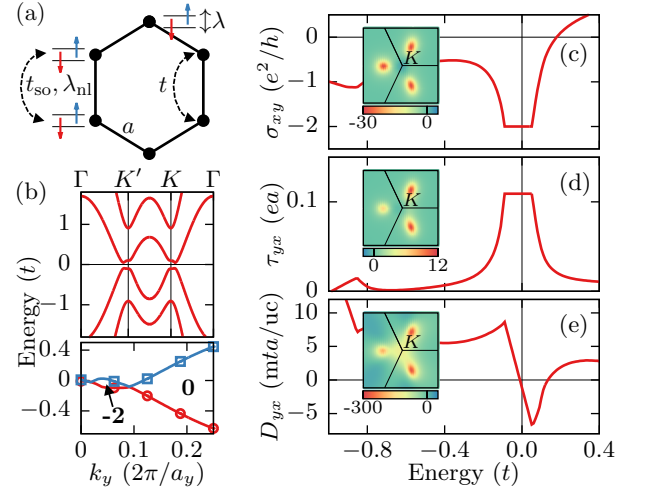


Figure 2. (Color online) (a) Sketch of the tight-binding model. (b) Top: Band structure of magnetically doped graphene with out-of-plane magnetization and $t_{\text{so}} = 0.3t$, $\lambda = 0.1t$, $\lambda_{\text{nl}} = 0.4t$. Bottom: Top of valence band (red circles) and bottom of conduction band (blue squares) in the (k_x, θ) -space. The bold integers denote the mixed Chern number \mathcal{Z} in the insulating regions, and $a_y = 3a/2$. (c)–(e) Energy dependence of the anomalous Hall conductivity $\sigma_{xy} = Ce^2/h = e^2/(2\pi h) \int \Omega_{xy}^{kk} dk_x dk_y$, the torkance τ_{yx} , and the spiralization D_{yx} , respectively, for an out-of-plane magnetization. Insets show the corresponding momentum-space distributions summed over all occupied states in the vicinity of the K -point.

to these effects. We point out intriguing perspectives for the electric-field control of magnetization in absence of longitudinal charge currents in these systems, which may ultimately lead to an ultralow power consumption of future spintronic devices exploiting SOTs.

Magnetically doped graphene.— We begin with a tight-binding model of magnetically doped graphene [30, 36]:

$$H = -t \sum_{\langle ij \rangle \alpha} c_{i\alpha}^\dagger c_{j\alpha} + it_{\text{so}} \sum_{\langle ij \rangle \alpha \beta} \hat{\mathbf{e}}_z \cdot (\boldsymbol{\sigma} \times \mathbf{d}_{ij}) c_{i\alpha}^\dagger c_{j\beta} + \lambda \sum_{i\alpha\beta} (\hat{\mathbf{m}} \cdot \boldsymbol{\sigma}) c_{i\alpha}^\dagger c_{i\beta} - \lambda_{\text{nl}} \sum_{\langle ij \rangle \alpha \beta} (\hat{\mathbf{m}} \cdot \boldsymbol{\sigma}) c_{i\alpha}^\dagger c_{j\beta}, \quad (3)$$

which is sketched in Fig. 2a. Here, $c_{i\alpha}^\dagger$ ($c_{i\alpha}$) denotes the creation (annihilation) of an electron with spin α at site i , $\langle \dots \rangle$ restricts the sums to nearest neighbors, the unit vector \mathbf{d}_{ij} points from j to i , and $\boldsymbol{\sigma}$ is the vector of Pauli matrices. Besides the usual hopping with amplitude t , the first line in Eq. (3) contains the Rashba spin-orbit coupling of strength t_{so} originating in the surface potential gradient of the substrate. The remaining terms in Eq. (3) are the exchange energy due to the local (λ) and non-local (λ_{nl}) exchange interaction between spin and magnetization. Depending on $\hat{\mathbf{m}}$, the non-local exchange describes a hopping process during which the spin can flip.

First, by monitoring the evolution of the mixed Chern number \mathcal{Z} we demonstrate that the above model hosts a mixed Weyl semimetal state. Indeed, as shown in Fig. 2b, the topological index \mathcal{Z} changes from -2 to 0 at a certain value of k_y ,

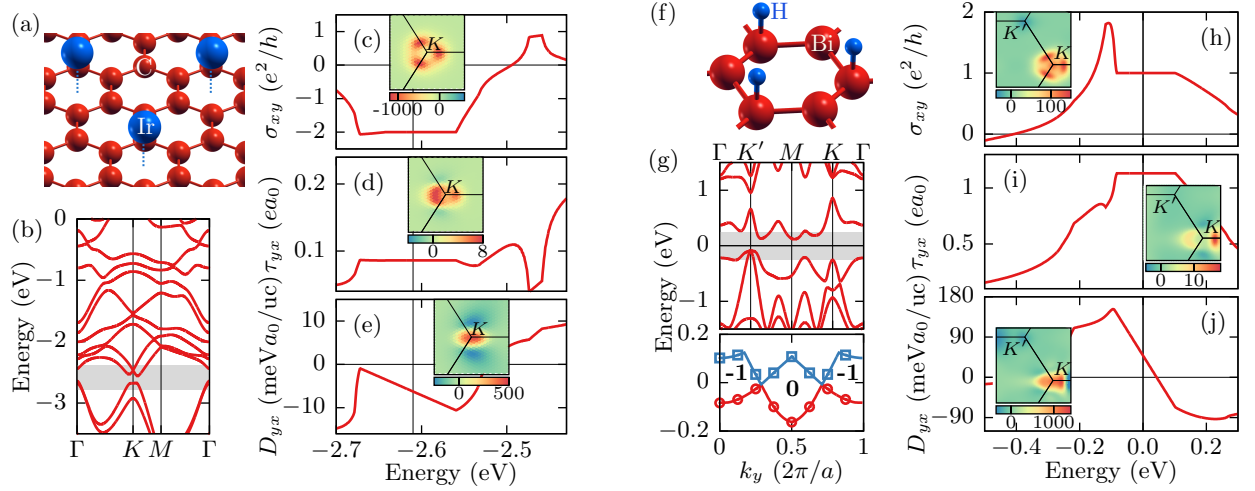


Figure 3. (Color online) (a) Crystal structure of graphene decorated by Ir adatoms in 2×2 geometry. (b) First-principles band structure of the system for an out-of-plane magnetization. The topologically non-trivial gap about 2.6 eV below the Fermi level is highlighted. (c)–(e) Energy dependence of anomalous Hall conductivity σ_{xy} , torkance τ_{yx} , and spiralization D_{yx} , respectively, for an out-of-plane magnetization. Vertical lines indicate the energy up to which states are summed up for the microscopic distributions in momentum space near the K -point, shown in the insets. (f) Crystal structure of the semihydrogenated Bi(111) bilayer. (g) Top: First-principles band structure of the system for an out-of-plane magnetization, where the region of the topologically non-trivial band gap is highlighted. Bottom: Evolution of top of valence band (red circles) and bottom of conduction band (blue squares) in the (k_x, θ) -space. Bold integers denote the mixed Chern number \mathcal{Z} , and a is the in-plane lattice constant. (h)–(j) Energy dependence of σ_{xy} , τ_{yx} , and D_{yx} for \hat{m} out of the plane.

indicating thus the presence of a band crossing in composite phase space that carries a topological charge of +2. One of these monopoles appears near the K -point off any high-symmetry line if the magnetization is oriented in-plane along the x -direction (see Fig. 1b). The emergence of the quantum anomalous Hall effect [36], Fig. 2c, over a wide range of magnetization directions can be understood as a direct consequence of the magnetic monopoles acting as sources of the curvature Ω^{kk} . Correspondingly, for \hat{m} out of the plane, the system is a quantum anomalous Hall insulator. Moreover, large values of the mixed curvature $\Omega^{\hat{m}k}$ in the vicinity of the monopole are visible in the momentum-space distributions of torkance and spiralization in the insets of Figs. 2d and 2e, respectively. For an out-of-plane magnetization, the primary microscopic contribution to the effects arises from an avoided crossing along ΓK – a residue of the Weyl point in (\mathbf{k}, θ) -space. Since the expressions (1) and (2) differentiate the wave function only with respect to one of the momentum coordinates, the symmetry between k_x and k_y in the distributions of torkance and spiralization is broken naturally.

As a consequence of the monopole-driven momentum-space distribution, the energy dependence of the torkance τ_{yx} , Fig. 2d, displays a decent magnitude of $0.1 ea$ in the insulating region (with a being the interatomic distance), and stays constant throughout the band gap. In contrast to the Chern numbers \mathcal{C} and \mathcal{Z} , the torkance τ_{yx} is, however, not guaranteed to be quantized to a robust value, i.e., the height of the torkance plateau in Fig. 2d is sensitive to fine details of the electronic structure such as magnetization direction and model parameters. Because of their intimate relation in the Berry phase theory [9, 37, 38], the plateau in torkance implies a linear be-

havior of the spiralization D_{yx} within the gap, changing from 8 mta/uc to -6 mta/uc as shown in Fig. 2e, where “uc” refers to the in-plane unit cell containing two atoms. We further explicitly confirm the origin of the large SOT and DMI in the monopoles by removing the Weyl points from the electronic structure via, e.g., including an intrinsic spin-orbit coupling term in Eq. (3), in which case the electric-field response in terms of torkance and spiralization is strongly suppressed.

To provide a realistic manifestation of the model considerations above, we study from *ab initio* the system of graphene decorated by 5d transition-metal adatoms. This system is known to realize the quantum anomalous Hall effect due to the spin-orbit mediated complex hybridization of graphene p states with d states of the transition metal [39]. In the case of Ir adatoms deposited on graphene (cf. Fig. 3a), a global band gap of 85 meV opens about 2.6 eV below the Fermi level if the magnetization is oriented out-of-plane, Fig. 3b. As visible in Fig. 3c, the system at this energy is a Chern insulator with $\mathcal{C} = -2$, where the main contribution to the Chern number comes from an avoided band crossing along KM . The magnitude of the torkance in the gap amounts to $\tau_{yx} = 0.1 ea_0$ (with a_0 being Bohr’s radius), Fig. 3d, and the spiralization D_{yx} ranges from -1 meV a_0 /uc to -10 meV a_0 /uc, Fig. 3e, values that are the same order of magnitude as those obtained in metallic magnetic heterostructures [5, 9] and non-centrosymmetric bulk magnets [16]. Since the details of the electronic structure can influence the value of the torkance in the gap, e.g., upon replacing Ir with other 5d transition metals such as W, the magnitude of the SOT and DMI can be enhanced drastically in the gapped regions of corresponding materials, according to our calculations.

Functionalized bismuth film.— While the SOT and DMI in magnetically doped graphene are comparable in magnitude to those in conventional metallic magnets, now we focus on a semihydrogenated Bi(111) bilayer with an out-of-plane magnetization, Fig. 3f, another mixed Weyl semimetal but for which gigantic effects can be realized. The system is a valley-polarized quantum anomalous Hall insulator [40] with a sizeable magnetic moment of $1.0 \mu_B$ per unit cell, and exhibits a large band gap of 0.18 eV at the Fermi energy as well as a distinct asymmetry between the valleys K and K' , Fig. 3g.

Analyzing the evolution of the mixed Chern number \mathcal{Z} as a function of k_y in Fig. 3g, we detect two magnetic monopoles of opposite charge that emerge at the transition points between the topologically distinct phases with $\mathcal{Z} = -1$ and $\mathcal{Z} = 0$. Alternatively, these crossing points and the monopole charges in the composite phase space could be identified by monitoring the variation of the momentum-space Chern number \mathcal{C} with magnetization direction. These monopoles, acting as sources of the general curvature Ω , occur at generic points near the valley K for $\theta = 43^\circ$ (see Fig. 1c) and in the vicinity of the K' -point for $\theta = 137^\circ$, respectively. For an out-of-plane magnetization, the complex nature of the electronic structure in momentum space manifests in the quantization of \mathcal{C} to ± 1 , Fig. 3h, which is primarily due to the pronounced positive contributions near K . Calculations of the energy dependence of the torkance and spiralization in the system, shown in Figs. 3i and 3j, reveal the extraordinary magnitudes of these phenomena of the order of $1.1 ea_0$ for τ_{yx} and $50 \text{ meV}a_0/\text{uc}$ for D_{yx} , exceeding by far the typical magnitudes of these effects in magnetic metallic materials [5, 9, 16]. As in the case of graphene, the SOT and DMI in this material are strongly suppressed if the Fermi energy is set to lie within the topologically trivial gaps that do not exhibit the mixed Weyl points.

Remarkably, the magnetization switching via anti-damping torques in mixed Weyl semimetals can be utilized to induce topological phase transitions from a Chern insulator to a trivial magnetic insulator mediated by the complex interplay between magnetization direction and momentum-space topology in these systems. In the case of the functionalized bismuth film, for instance, the material is a trivial magnetic insulator with a band gap of 0.25 eV if the magnetization is oriented parallel to the film plane. Nevertheless, the resulting anti-damping torkance $\tau_{yx} = 0.5 ea_0$ is still very large, and also the DMI varies from $D_{yx} = 105 \text{ meV}a_0/\text{uc}$ to $-60 \text{ meV}a_0/\text{uc}$ within the gap [30]. Overall, combining an exceptional electric-field response with a large band gap, the H-functionalized bismuth film serves as a distinct representative of a class of mixed Weyl semimetal materials, which lay out extremely promising vistas in room-temperature applications of magnetoelectric coupling phenomena for dissipationless magnetization control – a subject which is currently under extensive scrutiny (see, e.g., Refs. [29, 41, 42]).

In the examples that we considered here, the DMI changes over a wide range of values throughout the bulk band gap, implying that proper electronic-structure engineering enables us to tailor both strength and sign of the DMI in a given system,

for example, by doping or applying strain. Such versatility could be particularly valuable for the stabilization of chiral magnetic structures such as skyrmions in insulating ferromagnets. In the latter case, very large values of the anti-damping SOT arising in these systems would open exciting perspectives in manipulation and dynamical properties of chiral objects associated with minimal energy consumption by magnetoelectric coupling effects. Generally, we would like to remark that magnetic monopoles in the composite phase space, which we discuss here, do not only govern the electric-field response in insulating magnets but are also relevant in metals, where they appear on the background of metallic bands. Ultimately, in analogy to (non-quantized) anomalous Hall effect in metals, this makes the analysis of SOT and DMI in metallic systems very complex owing to competing contributions to these effects from various bands present at the Fermi energy. In addition, the electric-field strength in metals is typically much smaller, limiting thus the reachable magnitude of response phenomena as compared to insulators.

At the end, we comment on the relevance of the physics discussed here for antiferromagnets (AFMs) that satisfy the combined symmetry of time reversal and spatial inversion. SOTs in such antiferromagnets are intimately linked with the physics of Dirac fermions, which are doubly-degenerate elementary excitations with linear dispersion [43, 44]. In these systems, the reliable switching of the staggered magnetization by means of current-induced torques has been demonstrated very recently [8]. In analogy to the concept of mixed Weyl semimetals presented here, we expect that the notion of *mixed Dirac semimetals* in a combined phase space of crystal momentum and direction of the staggered magnetization vector will prove fruitful in understanding the microscopic origin of SOTs in insulating antiferromagnets. Following the very same interpretation that we formulated here for ferromagnets, monopoles in the electronic structure of AFMs can be anticipated to constitute prominent sources or sinks of the corresponding general non-Abelian Berry curvature, whose mixed band-diagonal components correspond to the sublattice-dependent anti-damping SOT, in analogy to the spin Berry curvature for quantum spin Hall insulators and Dirac semimetals [45–47]. Correspondingly, exploiting the principles of electronic-structure engineering for topological properties depending on the staggered magnetization could result in an advanced understanding and utilization of pronounced magnetoelectric response in insulating AFMs.

We gratefully acknowledge computing time on the supercomputers JUQUEEN and JURECA at Jülich Supercomputing Center as well as at the JARA-HPC cluster of RWTH Aachen, and funding under the HGF-YIG programme VH-NG-513 and SPP 1538 of DFG.

* j.hanke@fz-juelich.de

[1] A. Chernyshov, M. Overby, X. Liu, J. K. Furdyna, Y. Lyanda-

- Geller, and L. P. Rokhinson, *Nat. Phys.* **5**, 656 (2009).
- [2] I. M. Miron, G. Gaudin, S. Auffret, B. Rodmacq, A. Schuhl, S. Pizzini, J. Vogel, and P. Gambardella, *Nat. Mater.* **9**, 230 (2010).
- [3] I. M. Miron, T. Moore, H. Szabolcs, L. D. Buda-Prejbeanu, S. Auffret, B. Rodmacq, S. Pizzini, J. Vogel, M. Bonfim, A. Schuhl, *et al.*, *Nat. Mater.* **10**, 419 (2011).
- [4] K. Garello, I. M. Miron, C. O. Avci, F. Freimuth, Y. Mokrousov, S. Blügel, S. Auffret, O. Boulle, G. Gaudin, and P. Gambardella, *Nature Nanotech.* **8**, 587 (2013).
- [5] F. Freimuth, S. Blügel, and Y. Mokrousov, *Phys. Rev. B* **90**, 174423 (2014).
- [6] I. M. Miron, K. Garello, G. Gaudin, P.-J. Zermatten, M. V. Costache, S. Auffret, S. Bandiera, B. Rodmacq, A. Schuhl, and P. Gambardella, *Nature* **476**, 189 (2011).
- [7] L. Liu, O. Lee, T. Gudmundsen, D. Ralph, and R. Buhrman, *Phys. Rev. Lett.* **109**, 096602 (2012).
- [8] P. Wadley, B. Howells, J. Železný, C. Andrews, V. Hills, R. P. Campion, V. Novák, K. Olejník, F. Maccherozzi, S. S. Dhesi, S. Y. Martin, T. Wagner, J. Wunderlich, F. Freimuth, Y. Mokrousov, J. Kuneš, J. S. Chauhan, M. J. Grzybowski, A. W. Rushforth, K. W. Edmonds, B. L. Gallagher, and T. Jungwirth, *Science* **351**, 587 (2016).
- [9] F. Freimuth, S. Blügel, and Y. Mokrousov, *J. Phys.: Condens. Matter* **26**, 104202 (2014).
- [10] H. Kurebayashi, J. Sinova, D. Fang, A. C. Irvine, T. D. Skinner, J. Wunderlich, V. Novák, R. P. Campion, B. L. Gallagher, E. K. Vehstedt, L. P. Žárbo, K. Výborný, A. J. Ferguson, and T. Jungwirth, *Nature Nanotech.* **9**, 211 (2014).
- [11] I. Dzyaloshinsky, *J. Phys. Chem. Solids* **4**, 241 (1958).
- [12] T. Moriya, *Phys. Rev.* **120**, 91 (1960).
- [13] A. Neubauer, C. Pfleiderer, B. Binz, A. Rosch, R. Ritz, P. G. Niklowitz, and P. Böni, *Phys. Rev. Lett.* **102**, 186602 (2009).
- [14] N. Kanazawa, Y. Onose, T. Arima, D. Okuyama, K. Ohoyama, S. Wakimoto, K. Kakurai, S. Ishiwata, and Y. Tokura, *Phys. Rev. Lett.* **106**, 156603 (2011).
- [15] C. Franz, F. Freimuth, A. Bauer, R. Ritz, C. Schnarr, C. Duvinage, T. Adams, S. Blügel, A. Rosch, Y. Mokrousov, and C. Pfleiderer, *Phys. Rev. Lett.* **112**, 186601 (2014).
- [16] J. Gayles, F. Freimuth, T. Schena, G. Lani, P. Mavropoulos, R. A. Duine, S. Blügel, J. Sinova, and Y. Mokrousov, *Phys. Rev. Lett.* **115**, 036602 (2015).
- [17] N. Nagaosa, J. Sinova, S. Onoda, A. H. MacDonald, and N. P. Ong, *Rev. Mod. Phys.* **82**, 1539 (2010).
- [18] D. Xiao, J. Shi, and Q. Niu, *Phys. Rev. Lett.* **95**, 137204 (2005).
- [19] F. Freimuth, R. Bamler, Y. Mokrousov, and A. Rosch, *Phys. Rev. B* **88**, 214409 (2013).
- [20] Z. Fang, N. Nagaosa, K. S. Takahashi, A. Asamitsu, R. Mathieu, T. Ogasawara, H. Yamada, M. Kawasaki, Y. Tokura, and K. Terakura, *Science* **302**, 92 (2003).
- [21] M. Z. Hasan and C. L. Kane, *Rev. Mod. Phys.* **82**, 3045 (2010).
- [22] X.-L. Qi and S.-C. Zhang, *Rev. Mod. Phys.* **83**, 1057 (2011).
- [23] R. Yu, W. Zhang, H.-J. Zhang, S.-C. Zhang, X. Dai, and Z. Fang, *Science* **329**, 61 (2010).
- [24] C.-Z. Chang, J. Zhang, X. Feng, J. Shen, Z. Zhang, M. Guo, K. Li, Y. Ou, P. Wei, L.-L. Wang, Z.-Q. Ji, Y. Feng, S. Ji, X. Chen, J. Jia, X. Dai, Z. Fang, S.-C. Zhang, K. He, Y. Wang, L. Lu, X.-C. Ma, and Q.-K. Xue, *Science* **340**, 167 (2013).
- [25] G. Xu, H. Weng, Z. Wang, X. Dai, and Z. Fang, *Phys. Rev. Lett.* **107**, 186806 (2011).
- [26] S.-Y. Xu, I. Belopolski, N. Alidoust, M. Neupane, G. Bian, C. Zhang, R. Sankar, G. Chang, Z. Yuan, C.-C. Lee, S.-M. Huang, H. Zheng, J. Ma, D. S. Sanchez, B. Wang, A. Bansil, F. Chou, P. P. Shibayev, H. Lin, S. Jia, and M. Z. Hasan, *Science* **349**, 613 (2015).
- [27] B. Q. Lv, H. M. Weng, B. B. Fu, X. P. Wang, H. Miao, J. Ma, P. Richard, X. C. Huang, L. X. Zhao, G. F. Chen, Z. Fang, X. Dai, T. Qian, and H. Ding, *Phys. Rev. X* **5**, 031013 (2015).
- [28] D. Gosálbez-Martínez, I. Souza, and D. Vanderbilt, *Phys. Rev. B* **92**, 085138 (2015).
- [29] C. O. Avci, A. Quindeau, C.-F. Pai, M. Mann, L. Caretta, A. S. Tang, M. C. Onbasli, C. A. Ross, and G. S. D. Beach, *Nat. Mater.* (2016), 10.1038/nmat4812.
- [30] See Supplemental Material for computational details and magnetization dependence in the functionalized bismuth film.
- [31] J.-P. Hanke, F. Freimuth, S. Blügel, and Y. Mokrousov, *Phys. Rev. B* **91**, 184413 (2015).
- [32] A. A. Mostofi, J. R. Yates, G. Pizzi, Y.-S. Lee, I. Souza, D. Vanderbilt, and N. Marzari, *Comput. Phys. Commun.* **185**, 2309 (2014).
- [33] X. Wang, J. R. Yates, I. Souza, and D. Vanderbilt, *Phys. Rev. B* **74**, 195118 (2006).
- [34] J. R. Yates, X. Wang, D. Vanderbilt, and I. Souza, *Phys. Rev. B* **75**, 195121 (2007).
- [35] See <http://www.flapw.de>.
- [36] Z. Qiao, S. A. Yang, W. Feng, W.-K. Tse, J. Ding, Y. Yao, J. Wang, and Q. Niu, *Phys. Rev. B* **82**, 161414(R) (2010).
- [37] T. Thonhauser, *Int. J. Mod. Phys. B* **25**, 1429 (2011).
- [38] J.-P. Hanke, F. Freimuth, A. K. Nandy, H. Zhang, S. Blügel, and Y. Mokrousov, *Phys. Rev. B* **94**, 121114(R) (2016).
- [39] H. Zhang, C. Lazo, S. Blügel, S. Heinze, and Y. Mokrousov, *Phys. Rev. Lett.* **108**, 056802 (2012).
- [40] C. Niu, G. Bihlmayer, H. Zhang, D. Wortmann, S. Blügel, and Y. Mokrousov, *Phys. Rev. B* **91**, 041303 (2015).
- [41] Y.-H. Chu, L. W. Martin, M. B. Holcomb, M. Gajek, S.-J. Han, Q. He, N. Balke, C.-H. Yang, D. Lee, W. Hu, Q. Zhan, P.-L. Yang, A. Fraile-Rodriguez, A. Scholl, S. X. Wang, and R. Ramesh, *Nat. Mater.* **7**, 478 (2008).
- [42] D. Chiba, M. Sawicki, Y. Nishitani, Y. Nakatani, F. Matsukura, and H. Ohno, *Nature* **455**, 515 (2008).
- [43] P. Tang, Q. Zhou, G. Xu, and S.-C. Zhang, *Nat. Phys.* **12**, 1100 (2016).
- [44] L. Šmejkal, J. Železný, J. Sinova, and T. Jungwirth, *arXiv:1610.08107* (2016).
- [45] S. Murakami, *New J. Phys.* **9**, 356 (2007).
- [46] S. Murakami and S.-i. Kuga, *Phys. Rev. B* **78**, 165313 (2008).
- [47] B.-J. Yang and N. Nagaosa, *Nat. Commun.* **5**, 4898 (2014).

Supplemental materials for “Mixed Weyl semimetals and dissipationless magnetization control in insulators”

METHODS

First-principles calculations.— Using the full-potential linearized augmented plane-wave code `FLEUR` [35], we performed self-consistent density functional theory calculations of the electronic structure of (i) graphene decorated with Ir adatoms in 2×2 -geometry, and (ii) a semihydrogenated Bi(111) bilayer. The structural and computational parameters of Refs. [39] and [40] were assumed in the respective cases. Starting from the converged charge density, the Kohn-Sham equations were solved on an equidistant mesh of 8×8 \mathbf{k} -points for 8 different magnetization directions $\hat{\mathbf{m}} = (\sin \theta, 0, \cos \theta)$, where the angle θ covers the unit circle once. Based on the resulting wave-function information in the composite phase space, we constructed a single set of higher-dimensional Wannier functions (HDWFs) [31] for each of the systems by employing our extension of the `WANNIER90` code [32]. In case (i), we generated 82 HDWFs out of 120 energy bands with the frozen window up to 3.3 eV above the Fermi level, and in the case (ii), we extracted from 28 bands 14 HDWFs for a frozen window that extends to 2.1 eV above the Fermi energy.

We used the Wannier interpolation [33, 34] that we generalized to treat crystal momentum and magnetization direction on an equal footing [31] in order to evaluate the Berry curvatures $\Omega^{\mathbf{k}\mathbf{k}}$ and $\Omega^{\hat{\mathbf{m}}\mathbf{k}}$. Taking into account the above parametrization of the magnetization direction by θ , we were thus able to access efficiently the anomalous Hall conductivity σ_{ij} , the torkance τ_{yj} , and the spiralization D_{yj} :

$$\sigma_{ij} = \frac{e^2}{h} \frac{1}{2\pi} \int 2\text{Im} \sum_n^{\text{occ}} \left\langle \frac{\partial u_{\mathbf{k}n}}{\partial k_i} \left| \frac{\partial u_{\mathbf{k}n}}{\partial k_j} \right\rangle dk_x dk_y, \quad (\text{S1})$$

$$\tau_{yj} = e \int 2\text{Im} \sum_n^{\text{occ}} \left\langle \frac{\partial u_{\mathbf{k}n}}{\partial \theta} \left| \frac{\partial u_{\mathbf{k}n}}{\partial k_j} \right\rangle dk_x dk_y, \quad (\text{S2})$$

$$D_{yj} = \frac{1}{V} \int \text{Im} \sum_n^{\text{occ}} \left\langle \frac{\partial u_{\mathbf{k}n}}{\partial \theta} \left| h_{\mathbf{k}n} \frac{\partial u_{\mathbf{k}n}}{\partial k_j} \right\rangle dk_x dk_y, \quad (\text{S3})$$

with the same definitions as in the main text. Convergence of these quantities was achieved using 1024×1024 \mathbf{k} -points in the Brillouin zone. We obtained the mixed Chern number $\mathcal{Z}(k_y) = 1/(2\pi) \int 2\text{Im} \sum_n^{\text{occ}} \langle \partial_\theta u_{\mathbf{k}n} | \partial_{k_x} u_{\mathbf{k}n} \rangle d\theta dk_x$ by integrating the mixed Berry curvature on a uniform mesh of 1024 k_x -values and 512 angles θ in $[0, 2\pi)$.

Tight-binding model.— To arrive at the Hamiltonian (3) of the main text, the model in Ref. [36] has been generalized to account for arbitrary magnetization directions $\hat{\mathbf{m}}$ and the non-local exchange interaction. We obtained a 4×4 -matrix

representation of the Hamiltonian (3) on the bipartite lattice of graphene by introducing four orthonormal basis states $|N\alpha\rangle$ that describe electrons with spin $\alpha = \{\uparrow, \downarrow\}$ on the sublattice $N = \{A, B\}$. Using Fourier transformations, we transformed this matrix to a representation $H(\mathbf{k})$ in momentum space, which was subsequently diagonalized at every \mathbf{k} -point to access the electronic and topological properties of the system. The model parameters $t_{\text{so}} = 0.3t$, $\lambda = 0.1t$, and $\lambda_{\text{nl}} = 0.4t$ were employed in this work. We chose the magnetization direction as $\hat{\mathbf{m}} = (\cos \theta, 0, \sin \theta)$ for a direct comparison between the model and the first-principles calculations.

SEMIHYDROGENATED BISMUTH FILM: ANISOTROPY WITH MAGNETIZATION DIRECTION

In Fig. S1, we show the dependence of anomalous Hall conductivity, torkance, and spiralization on the magnetization direction $\hat{\mathbf{m}} = (\sin \theta, 0, \cos \theta)$ in the semihydrogenated bismuth film. For general magnetization directions, both torkance and spiralization display also small non-zero components τ_{yy} and D_{yy} , respectively, since the shape of these response tensors is dictated by the crystal symmetries and not due to Onsager’s reciprocity relations. When the Weyl point emerges in the electronic structure at $\theta = 43^\circ$, the system undergoes a topological phase transition from a Chern insulator to a trivial magnetic insulator, which is accompanied by a jump in σ_{xy} and a similar drop of τ_{ij} . As apparent from Fig. S1, the torkance τ_{yx} is still remarkably prominent in the regime of the trivial insulator, i.e., for $\theta > 43^\circ$.

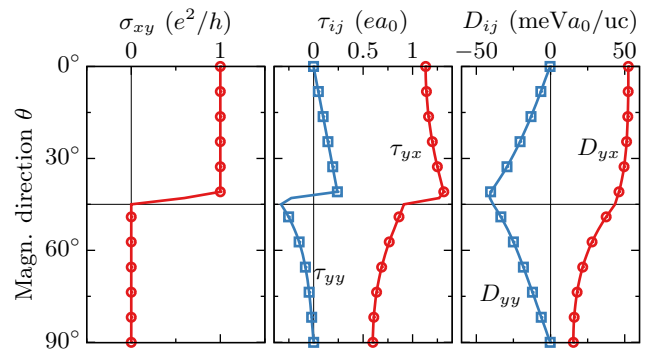


Figure S1. The anomalous Hall conductivity σ_{xy} , the torkance τ_{ij} , and the spiralization D_{ij} at the actual Fermi level in the semihydrogenated bismuth film as a function of the magnetization direction $\hat{\mathbf{m}} = (\sin \theta, 0, \cos \theta)$. The Weyl point in the electronic structure emerges at $\theta = 43^\circ$.